37TH AIAA Fluid Dynamics Conference and Exhibit
AIAA 2007-4490

Comparisons of Transition Prediction using PSE-Chem to Measurements for a Shock Tunnel Environment

Matthew MacLean*
Erik Mundy*
Timothy Wadhams*
Michael Holden†
CUBRC, Aerothermal/Aero-optics Evaluation Center, Buffalo, NY, 14225

Heath Johnson‡
Graham Candler§
Department of Aerospace Engineering and Mechanics
University of Minnesota, Minneapolis, MN 55455

Predictions from the STABL code have been used to make comparisons to two series of fundamental transition experiments in a large-scale shock tunnel environment by solving the parabolized stability equations (PSE) to predict laminar-turbulent transition onset using a semi-empirical e^N correlation. The two sets of experimental data were obtained at duplicated enthalpy Mach 10 conditions for slender geometries where transition is dominated by second-mode instability. The first experiment considered is a 7^O cone with sharp and blunt nosetips where the surface pressure gradient is zero and the second is an axisymmetric compression surface with a significant adverse pressure gradient acting upon the flow. The PSE analysis has predicted N-factor growth between 5.2 and 8.6 at the measured transition station for these cases, demonstrating a range of instability conditions describing the physical phenomena. The use of the Re_θ/M_E criterion is also explored, including examples on the axisymmetric compression surface where a low value indicating early transition shows the opposite trend to the more physically accurate PSE solution that indicates larger N-factor growth.

I. Introduction

Current hypersonic vehicle design methodologies typically rely on incomplete and limited sources of information to understand one of the most critical issues governing the assessment of vehicle performance and safety. For both internal and external aerodynamics applications, laminar-turbulent transition effects remain one of the most significant drivers of vehicle design requirements. Transition behavior will have a large influence on heating rates, drag, separated region structure, control surface effectiveness, shock-boundary layer interactions, etc. Because of the large uncertainties in vehicle design requirements incurred as a result of the physics of transition, accurate prediction and testing of these effects for relevant flow conditions and geometries are critical. The LENS facilities have represented a major upgrade in the nation's testing capabilities in the past 20 years to study the effects of transition and turbulent aerothermodynamics by testing at fully-duplicated flow conditions on large size (often full-scale) vehicles from scramjets to interceptors to reentry bodies. To complement this existing experimental capability, we are beginning to integrate predictive tools to better design the experiments and to understand the acquired experimental data. Toward this end, we have started to employ the parabolized stability solver, *STABL*, from the University of Minnesota to predict the onset of laminar-turbulent transition on fundamental shapes to both enhance our understanding of the prediction of this phenomenon and to better interpret the experimental results in the framework of the ground test facility environment.

* Senior Research Scientist, AIAA Member.
†AAEC Program Manager, AIAA Fellow.
‡Senior Research Associate, AIAA Senior Member.
§Professor, AIAA Associate Fellow.

In this paper, we present comparisons of the predictions of STABL to the results obtained from experimental studies in the LENS-I facility for two geometries that were employed to provide fundamental transition data. In the first case, a 7^O cone was studied at zero degrees angle of attack with sharp and blunted nose tips. Downstream of the nose, the boundary layer is a zero pressure gradient flow. In the second case, an axisymmetric isentropic compression surface was studied with sharp and blunted nose tips. For this geometry, the flow is acted upon by a significant adverse pressure gradient, which often lends itself to augmented instability. This fundamental flowfield is representative of a flowfield like a scramjet inlet, where transition is a critical issue in the system design. These two models are shown in Fig. 1. These two flowfields are high edge Mach number, cold wall flows where we expect the transition process to be dominated by second-mode instability.

(a) Cone Model *(b) Axisymmetric Compression Surface Model*

Figure 1. Fundamental Transition Experiments Performed in the LENS-I Facility.

In previous work, we have relied on correlations like Re_θ/M_E to estimate a transition onset point for the purposes of design-of-experiment. For both of these studies, we compare the prediction capabilities of an Re_θ/M_E correlation and PSE solution to sufficiently distinguish the effects of the varying nose bluntness or the effects of the adverse pressure gradient on the measured instability in the ground test environment.

II. Experimental Facility Background

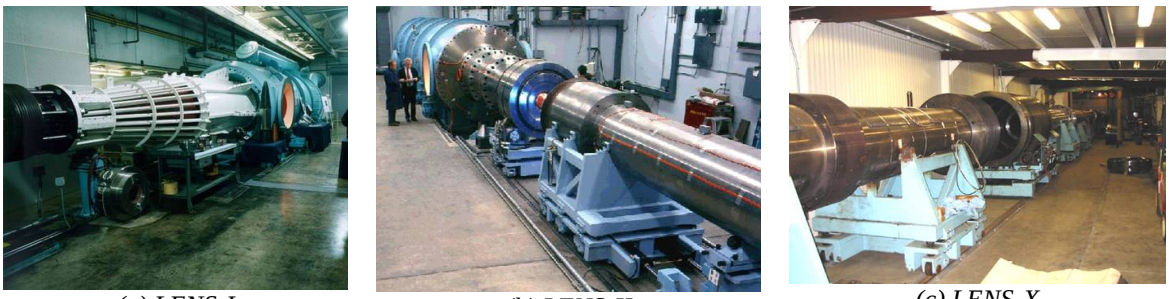

(a) LENS-I *(b) LENS-II* *(c) LENS-X*

Figure 2. LENS Facilities at CUBRC

Currently, CUBRC operates the 48" reflected shock tunnel, the LENS-I and LENS-II reflected shock tunnels[1], and the LENS-X expansion tunnel[2] shown in Fig 2. The reflected shock tunnel uses incident and reflected shocks to cleanly heat and pressurize a stagnant test gas to high enthalpy levels. This test gas may then be expanded through a converging-diverging nozzle in a manner similar to a blowdown facility to produce a hypervelocity test flow. Expansion tunnels like LENS-X also operate as short duration facilities, but an expansion tunnel produces a high enthalpy flow without the need to first stagnate the test gas. In an expansion tunnel, the high enthalpy test gas is generated in two stages – first by performing a small amount of heating and compression of the test gas with a single incident shock and then by further accelerating it with an unsteady expansion to add kinetic energy to the flow directly. The result is a low static temperature, high velocity test gas at a quiescent thermodynamic state like

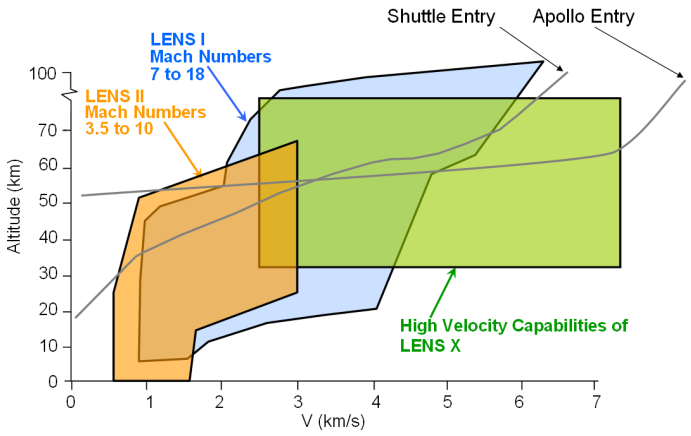

Figure 3. Velocity-Altitude Duplication Capabilities of CUBRC LENS Facilities

that of a flight condition. The freestream flow, which can be expanded to any test Mach number, is free of frozen, dissociated chemical contamination that can occur in the freestream of reflected shock facilities at very high enthalpies. CUBRC employs both reflected shock and expansion tunnels to provide a wide range of supersonic, hypersonic, and hypervelocity test capabilities, which are summarized in Fig 3.

The LENS reflected shock-tunnel facilities were developed primarily to study the full-scale, hypervelocity flow physics of interceptors and air-breathing engine configurations. The scale and flow duplication capabilities of LENS are such that these vehicles can be studied at their full scale, inclusive of effects such as transition to turbulence, turbulent mixing from cross-flow jets and thrusters, duplicated flow chemistry, and other effects that are difficult or impossible to simulate at cold-flow or sub-scale conditions. Besides aerothermal measurements, extensive studies in this facility have been made using non-intrusive diagnostics such as aero-optic and aero-acoustic measurements, including recent work with tunable laser-diode diagnostics[3,4]. The capabilities of LENS-I duplicate the flight conditions of interceptors and scramjet engines from Mach 7 to 15 (with Reynolds number matching to Mach 22), while the LENS-II facility complements it in such a way that this capability is seamlessly extended down to Mach 3.5 at sea level density.

III. Supporting Numerical Tools

A. DPLR Navier-Stokes Solver

All ground test studies in the LENS facilities are extensively calibrated and validated with numerical tools. The primary CFD tool used is the DPLR code provided by NASA Ames Research Center. DPLR is a multi-block, structured, finite-volume code that solves the reacting Navier-Stokes equations including finite rate chemistry and finite rate vibrational non-equilibrium effects. This code is based on the data-parallel line relaxation method[5] and implements a modified (low dissipation) Steger-Warming flux splitting approach[6] for the convection terms and central differencing for the diffusion terms. Finite rate vibrational relaxation is modeled via a simple harmonic oscillator vibrational degree of freedom[7] using the Landau-Teller model[8]. Vibrational energy relaxation rates are computed by default from the semi-empirical expression due to Millikan and White[9], but rates from the work of Camac[10] and Park, et al[11] are substituted for specific collisions where experimental data exists. Vibration-dissociation coupling is currently modeled using the *T-Tv* approach of Park[12] or with some preliminary implementation of CVDV coupling[13]. Transport properties are appropriately modeled in DPLR for high enthalpy flow[14,15] using the binary collision-integral based mixing rules from Gupta, et al[16]. Diffusion coefficients are modeled using the self-consistent effective binary diffusion (SCEBD) method[17]. Turbulence models available in the DPLR code currently include the Baldwin-Lomax 0-equation model[18], the Spalart-Allmaras model 1-equation model[19], and the Shear Stress Transport (SST) 2-equation model[20] each with corrections for compressibility effects[21,22]. Recent relevant capabilities of the DPLR code involve automated grid adaptation to improve solution quality[23].

B. STABL Tool Package/PSE-Chem Solver

The Stability and Transition Analysis for Hypersonic Boundary Layers (STABL) package[24,25,26] is a comprehensive suite of tools that features an integrated two-dimensional/axisymmetric chemically reacting laminar flow solver, equilibrium chemistry solver, parabolized stability solver, post-processor and various supporting tools and scripting wizards integrated into a single, intuitive, Perl-based GUI interface. The CFD and PSE solvers use MPI for efficient parallel processing. STABL is developed at the University of Minnesota (a combination of versions 2.4 and 2.6 were used for these analyses).

The PSE-Chem solver is a primary part of the STABL suite that solves the parabolized stability equations for two-dimensional or axisymmetric flow derived from the Navier-Stokes equations. The PSE equations are developed by modeling instantaneous flow variables with a mean and fluctuating component and subtracting the mean component from the resulting equation set. The result is a system of 2nd order partial differential equations for the disturbances, which are parabolized according to the method of Herbert[27] by assuming that the disturbances are composed of a fast-oscillatory wave part and a slowly-varying shape function. The ellipticity of the wave part is preserved while only the governing equation for the shape function is parabolized. Assuming that initial disturbances are small and making an assumption of "locally-parallel" flow at the starting plane allows sufficient simplification to generate an initial solution for the shape function and complex streamwise wavenumber. These initial solutions may then be marched downstream by integrating the parabolized stability equations.

The PSE analysis generates a prediction for the evolution of an initial disturbance as it moves downstream from its starting point through the mean flowfield. To predict the onset of transition, an experimental correlation is required. PSE-Chem uses the semi-empirical e^N correlation method, where N is defined by:

$$N(\omega, s) = \int_{s0}^{s} \left[-\mathrm{Im}(\alpha) + \frac{1}{2E}\frac{dE}{ds} \right] ds$$

Experimental studies have shown N to be about 8 – 11 for quiescent flight environments and levels around 5.5 (sometimes lower) for tunnel environments where freestream noise levels can be somewhat larger.

C. Integration of the Tools

Although the STABL package includes a reasonably full-featured CFD solver and various other supporting tools as part of its distribution, the DPLR code discussed in §III-A was chosen to compute the mean flowfields required for the PSE stability analysis. This decision was made largely because of the prior familiarity with the DPLR code operation and interfacing, minimizing the learning time required to obtain results. DPLR also has several features that were not available in the STABL CFD solver at the time of this analysis like automated shock adaptation and a variety of chemical and transport models. Although this decision saved considerable time by not having to learn a new CFD mean flow solver, it simultaneously created a new step in that the DPLR solution file had to be converted to provide the required input to PSE-Chem which consists of the variable set (x, y, $\rho_{1\text{-}N}$, u, v, T, T_V). The DPLR post-processor (*postflow*) can output all of these variables directly from the restart file information, but the finite volume scheme computes the solution variables at cell centers which do not coincide with spatial grid point locations. There are several options available in postflow to rectify this, and the transfer was made using the option "interpolate grid points to cell centers, but include values at face edges too" (*interp=1*) which is consistent with the arrangement of the input expected by PSE-Chem. Using postflow as an intermediate, it was possible to efficiently convert the DPLR solution to be compatible with solutions as generated by the built-in STABL solver.

Also noted here is the calculation of the boundary layer characteristic parameters used to compare to the PSE-Chem solutions (e.g. boundary layer thickness, $\mathrm{Re}_\theta/\mathrm{M}_E$, etc.). These quantities were extracted with a separate code directly from the DPLR mean flow solution assuming an edge definition of 99.5% freestream total enthalpy for all cases.

IV. Experiment I: Axisymmetric Cone (Zero Pressure Gradient Flow)

A. Overview of Experimental Studies and Model Geometry

The cone geometry was studied over a range of conditions at Mach numbers 7 and 10 in two different nozzles in the LENS-I facility (C nozzle and D nozzle) to provide fundamental transition data in a zero pressure gradient flow for two different noise-level environments. Nosetips of several sizes (including sharp) were employed to assess bluntness effects due to entropy layer stabilization. In the shock tunnel environment, the wall is consistently at room temperature (300K). The model is shown installed in the tunnel in Fig 4.

Figure 4. Photograph of Cone Model Installed in Facility

The geometry of this model is a 7^O cone which is 2.35-m in axial length. All stations are referenced from the sharp tip at X=0.0 (thus cases with a blunt nose start at some small positive X station). Experimental data, CFD mean flow solutions, and PSE solutions are all referenced consistently in this way. Instrumentation on the model consists of four rays of thin-film heat transfer gages located at 0^O, 90^O, 180^O, and 270^O around the model. Since all cases considered here were tested with the model at 0^O angle of attack, the instrumentation is a check of consistency of flow conditions, accuracy of model attitude, and – most importantly – variation in the physical transition process.

After a brief review of the Mach 7 cases considered in earlier published work[28], the focus of the results presented here will be on the Mach 10 cases.

B. Review of Mach 7 PSE-Chem Analysis

Earlier work[28] on these experimental studies detailed STABL results for some cases at both Mach 7 and Mach 10. Here, we cite the results and discussion shown there and provide only a brief review of some important results for the framework of this discussion. The main runs of this study were obtained at two different Mach numbers of

6.58 and 7.15 each with two different nose radius shapes of 2.5-mm and 5.0-mm for a total of four runs demonstrating the effect of Mach number and the effect of nose radius on the transition process.

The major result of this part of the study is shown in Fig 5, which shows measured heat transfer rate compared to a laminar heating prediction from the DPLR simulation and the N-factor growth envelope from the PSE solution for each of the four cases. The calculations were computed independently of Ref [28] by the lead author, but the results obtained are the same for these cases as was reported there. For each run, a transition location was estimated as described elsewhere in this paper and this location is marked with a yellow window indicating a range of probable onset positions. If the center of the range is assumed to be the onset point for each run, then the N-factor at this station ranges from 4.75 to 6.6 with an average of about 5.5. This is close to the values reported by many ground test facilities with typical noise levels in the flow[29,30]. For these same cases, the value of Re_θ/M_E ranges from 120 to

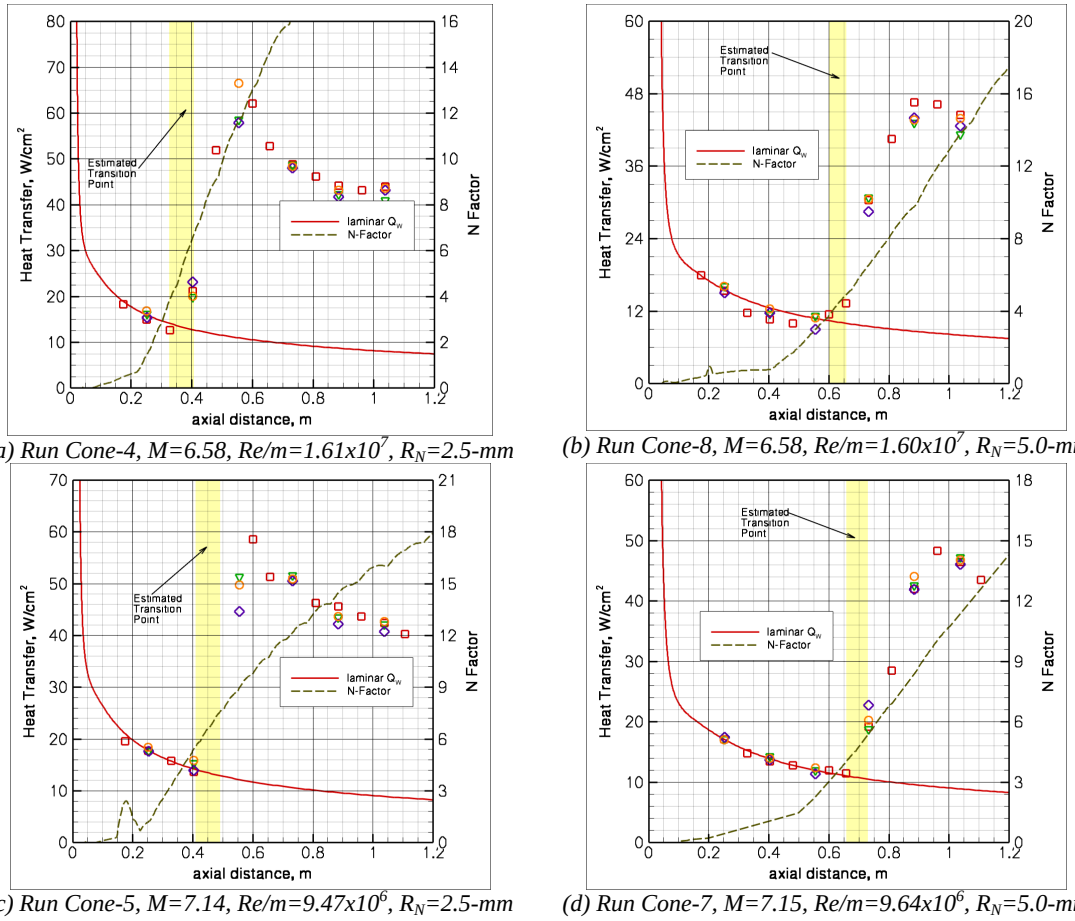

(a) Run Cone-4, M=6.58, Re/m=1.61x10⁷, R_N=2.5-mm

(b) Run Cone-8, M=6.58, Re/m=1.60x10⁷, R_N=5.0-mm

(c) Run Cone-5, M=7.14, Re/m=9.47x10⁶, R_N=2.5-mm

(d) Run Cone-7, M=7.15, Re/m=9.64x10⁶, R_N=5.0-mm

Figure 5. Comparison of Heat Transfer Prediction with Experiment and N-Factor Growth Prediction for Four Runs on a 7° Cone Model

220. Thus, while there is some variation in the levels of the N-factor prediction at the measured transition location from run to run, the range of values to obtain agreement with experiment is much smaller than with the traditional Re_θ/M_E metric. More discussion will follow in a later section, but it is also worthwhile to note that an N-factor of 10 indicative of a typical transition location in flight is only about 10-20 cm aft of the measured locations, so the possible range of transition locations from a very low N-factor to a very high one is well bounded for this flow.

C. Mach 10 PSE-Chem Analysis Results

Data from five runs at a nominal Mach 10 were measured on the cone model. It should be noted that these runs were performed at duplicated total enthalpy levels for Mach 10 flight of approximately 4.5 MJ/kg, which is considerably higher than the enthalpy required to simulate Mach 10 under cold flow conditions only. The mean flow is mildly chemically reacting at this energy level, which does have a slight destabilizing effect on the PSE instability growth[28]. In this series, three runs employed nosetips of sharp, 2.5-mm, and 6.35-mm with the same nominal test conditions. The sharp nosetip and the 6.35-mm nosetip were also used at a different Reynolds number

each. Results from the five cases look similar to each other, so Run Cone-19 employing the 2.5-mm nose at a unit freestream Reynolds number of 2.51×10^6 per meter is used as a typical case with results from the other runs summarized at the end of the section.

For a 512x256 cell grid, the chemically reacting mean flow equations were solved to convergence using DPLR. The grid was shock-adapted to the bow shock to improve the solution quality, and the near wall spacing was adjusted to enforce a cell Reynolds number of about 1.0 at the wall, which has been shown to produce accurate heat transfer prediction[31]. The new grid point distribution provides a fine spacing and many points in the boundary layer of the mean flow for STABL. Comparison with the measured heat transfer is shown in Fig 6. In the laminar region, excellent agreement is obtained for this high energy flow. Based on the information available, we estimate transition onset to have occurred at an axial station of approximately 1.1-m. The necessary mean flow solution quantities from DPLR were imported into the STABL binary XDR format. One of the features of the STABL toolkit is an object-oriented, graphical interface written in PERL. This feature allows the creation of a PSE test matrix graphically. Points are selected in a region around the estimate of the most unstable frequency for second

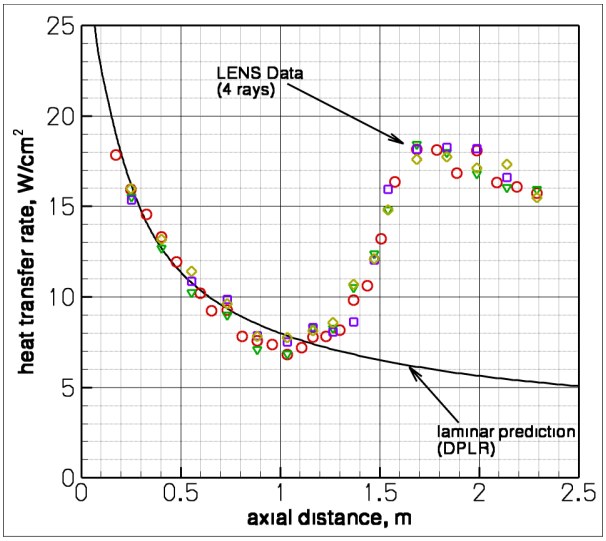

Figure 6. Measured Heat Transfer Distribution and DPLR Prediction for Run Cone-19

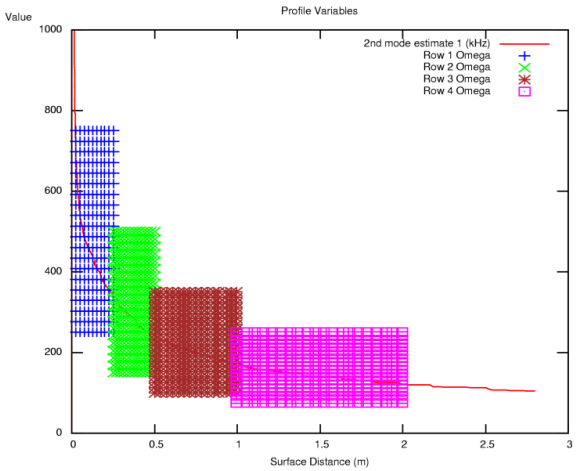

Figure 7. STABL Planner Test Matrix for Run Cone-19

mode transition as a function of axial station. The map of test points for Run Cone-19 is shown in Fig 7. The second mode instability estimate shown is computed in STABL by integrating the time of travel from the surface to the sonic line of the boundary layer, which is more accurate than the commonly used estimate equal to one-half edge velocity divided by boundary layer thickness. The PSE equation solver itself is a parallel code employing MPI and runs via a command line script.

The stability map of N-factors computed by STABL for all test points is shown in Fig 8. This map, given as a function of axial position, shows the growth and decay of each test point considered. For this flowfield, unstable disturbances grow most rapidly when they are nearest to the second mode eigenvalue frequency at that station. As the boundary layer grows and the second eigenmode changes, those same disturbances decay. The N-factor map also highlights the effect of the entropy gradient of the blunt nose which heavily suppress instability growth until 0.2-m when the entropy layer is sufficiently swallowed by the boundary layer. This effect is implicitly accounted for in the solution of the PSE equations.

STABL extracts the bounding curve of the most unstable frequency at a given axial station, which is shown in Fig 9. At the measured transition onset location of 1.1-

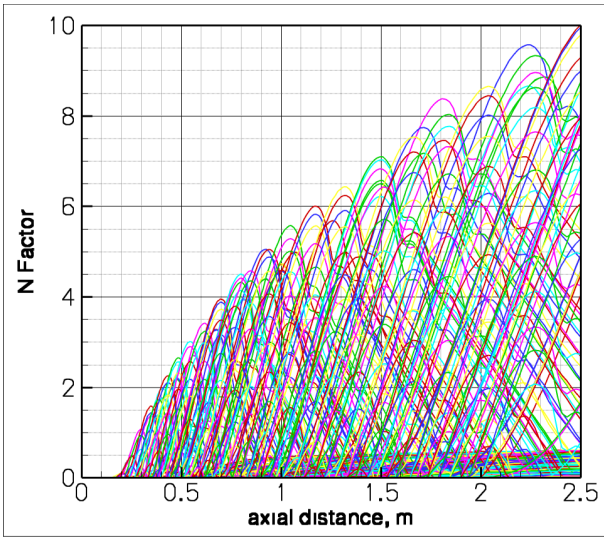

Figure 8. N-Factor Instability Map for Run Cone-19

m, the instability growth has reached a value of N=5.8 and the peak instability frequency is at 228 kHz. From the original DPLR mean flow solution, it is also possible to extract boundary layer edge properties for this flowfield by searching outward from the surface at each wall station. The edge Mach number and the value of Re_θ/M_E is shown in Fig 10. For the transition onset point, this value is 79, which is significantly lower than any of the values found for the Mach 7 cases in the previous section. For those conditions, values of Re_θ/M_E from 120 to 160 were obtained for the same nose radius geometry, indicating that this particular empirical correlation does not hold across such different flow conditions even for the same geometry.

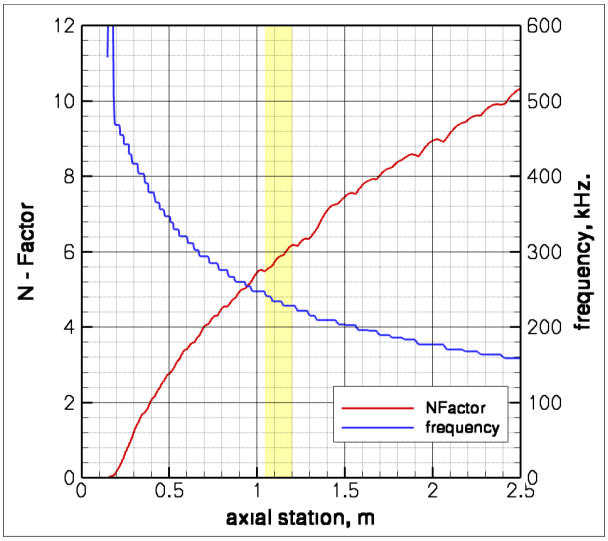

Figure 9. Instability (N-Factor) Envelope and Frequency for Run Cone-19 (transition at 1.05-1.2 m)

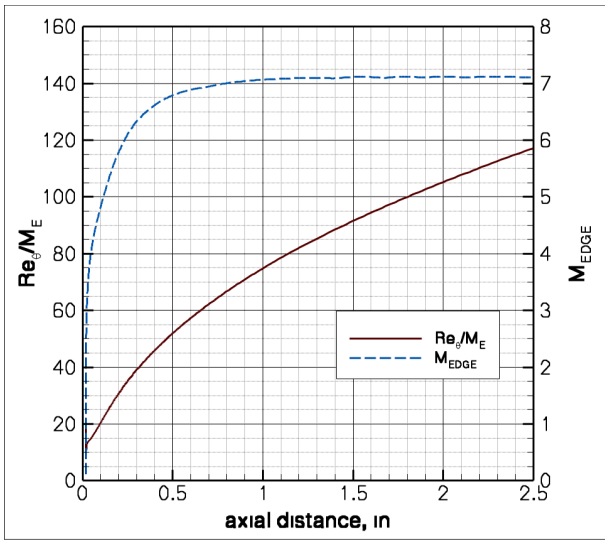

Figure 10. Edge Mach Number and Re_θ/M_E for Run Cone-19 (transition at 1.05-1.2 m)

The other four runs in this test series were computed in the same way as Run Cone-19 and similar types of results were obtained for each case. Relevant results including N-factor at the estimated transition point, frequency of maximum instability at that station, local Reynolds number at transition based on surface running length, and Re_θ/M_E are given along with freestream conditions in Table 1. Analysis of the results shows that there is a larger range of transition N-factors (5.2 to 7.0) for this set of runs than there were for the Mach 7 cases and the average is somewhat higher. The variability seems to occur with no correlation to the instability frequency but does correlate with the nose radius size, where the sharp nose configuration transitions at the lowest N-factor levels and increases with nose radius size. However, this variability is still much more tightly bounded than the Re_θ/M_E parameter which varies by as much as 46% across the five runs. It is interesting to point out that Reshotko[32] argues that the Re_θ/M_E parameter is essentially a correlation of the altitude of flight because the major dependency on it is density.

Table 1. Summary of Stability Analysis for Mach 10 Cone Studies

Run #	Nose radius (mm)	Mach number	Freestream unit Reynolds number x10^6 (m^{-1})	Transition location (axial) (m)	Instability N-factor at transition	Max-N Instability frequency (kHz)	Transition point local edge Reynolds number x10^6	Re_θ/M_E
Cone-18	6.35	9.90	2.363	1.65	6.6	190	3.74	95
Cone-19	2.50	9.95	2.339	1.13	5.8	228	2.82	79
Cone-20	sharp	9.92	2.416	0.90	5.2	261	2.50	73
Cone-21	6.35	9.93	3.129	1.50	7.0	225	4.31	104
Cone-22	sharp	10.01	1.793	1.10	5.2	200	2.26	69

Comparing runs Cone-18/21 or Cone-20/22 supports this conclusion exactly. In both instances, only the Reynolds number was varied keeping all other parameters including geometry the same. This implies that only the density changed in the freestream flow of the facility, while velocity and temperature were held constant. The local Reynolds number based on edge conditions and the Re_θ/M_E at the transition location is consistent for that particular parametric. However, when nose radius changes (comparing runs 18–20) or when the enthalpy of the flow changes (comparing run 4–8 to runs 18–22), then Re_θ/M_E does not correlate this dataset.

V. Experiment II: Axisymmetric Contoured Compression Surface (Adverse Pressure Gradient Flow)

A. Overview of Experimental Studies and Model Geometry

The axisymmetric compression surface is an Oswatitsch-type compression inlet design without an outer, annular collar to straighten the flow at the focal point of the isentropic compression waves. The Oswatitsch inlet is an annular equivalent of a Busemann inlet (axisymmetric, inward-turning) or a Prandtl-Meyer inlet (two-dimensional). The design of this inlet was based on a modification of the technique of Molder, et al.[33] which uses axisymmetric method of characteristics to trace the inlet surface. Like most isentropic inlets for hypersonic flow, the ideal inlet becomes very long so a small truncation (~0.5^O) was built into the inlet to significantly shorten the length. This makes the size of the inlet more realistic for application and reduced the difficulty to machine the narrow tip. While a modification to account for the rotational flow effects of a blunt, inviscid leading edge can be easily incorporated into the raytracing process, CFD results of both the inviscid and laminar flowfield showed that this correction was not necessary. The surface heating and pressure predicted for the design shape is shown in Fig 11. The smooth variations do not show any discontinuities indicative of a shock. Experimental studies in the LENS-I facility showed that the truncated and blunted leading edge did not significantly impact the flowfield as smooth isentropic compression waves were observed with Schelieren photography. For both laminar and turbulent flows, the boundary layer remains thin enough on the cold surface of the model that the inviscid flow is not affected by viscous effects at the Reynolds numbers studied. The compression surface is shown in Fig 12.

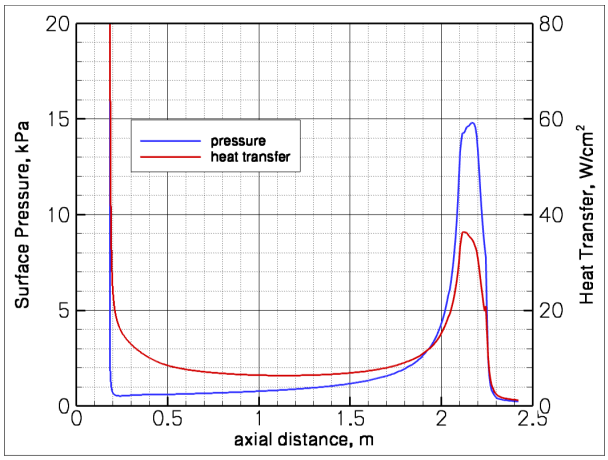

Figure 11. Prediction of Surface Heating and Pressure of Isentropic Design

The run matrix for this study in the LENS-I facility consisted of tripped and un-tripped (natural transition) runs. All cases were run at approximately Mach 10 with true temperature duplicated conditions. The total enthalpy of the flow is approximately 4.5 MJ/kg, which can be compared with the cone of experiment I in §IV. Two effects were primarily studied – Reynolds number effects by varying the freestream dynamic pressure from 13-kPa to 53-kPa, and the influence of nose bluntness by varying the nose radius from 1.27-mm to 6.35-mm with threaded, removable nosetips. In the case of this model, the axial distance is measured consistently from an arbitrary point in space in front of the model (since there is no sharp nosetip) so that larger nose radius configurations begin at larger X stations. The model instrumentation consists of three rays of thin-film heat transfer gages located at 0^O, 90^O, and 180^O. As with the cone model, at zero degrees angle of attack these rays provide nominally redundant measurements but serve to demonstrate the range of transition onset locations around the circumference of the axisymmetric flowfield.

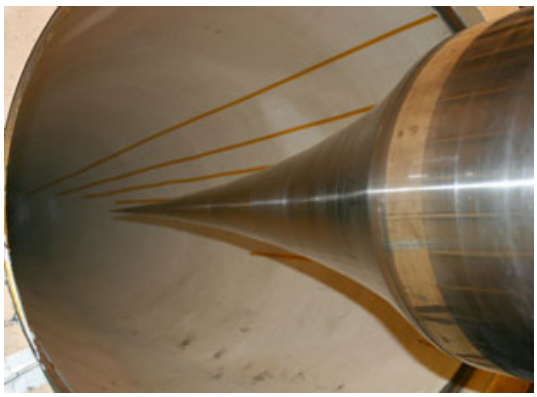

Figure 12. Photograph of Axisymmetric Compression Model in Facility

B. Grid Generation & CFD Analysis

Results of the CFD computation are best shown with a computational Schlieren image created by plotting density gradient magnitude of the axisymmetric flowfield. This is shown in Fig 13. Significant features observable include the weak bow shock which passes on the outside of the isentropic compression waves. The isentropic waves themselves coalesce at a point near the shoulder of the surface. In order to make use of some existing hardware, a compromise was made by blending in an existing shoulder rather than continuing the isentropic shape. The result of this is a weak oblique shock that occurs as noted on Fig 13. This occurs at 2.1-m axial station, so it is downstream of the transition zone of study and not important to the experiment. A calculation of boundary layer thickness is presented in Fig 14, showing the contrasting behavior of this flowfield to the viscous development on the cone surface. Here, the adverse pressure gradient suppresses boundary layer growth to such an extent that the boundary layer thickness reaches a maximum at X=1.0m and then begins to decrease over the second half of the model.

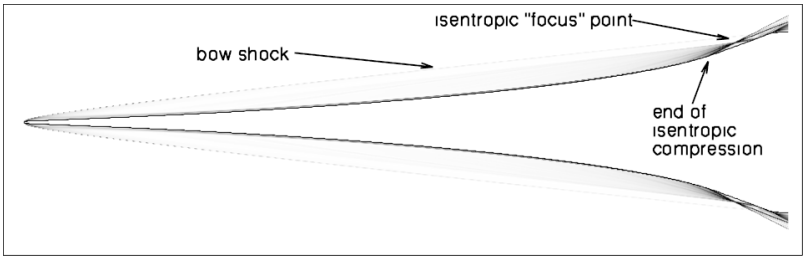

Figure 13. DPLR Prediction of Axisymmetric Compression Model showing Contours of Density Gradient Magnitude and Major Shock Features

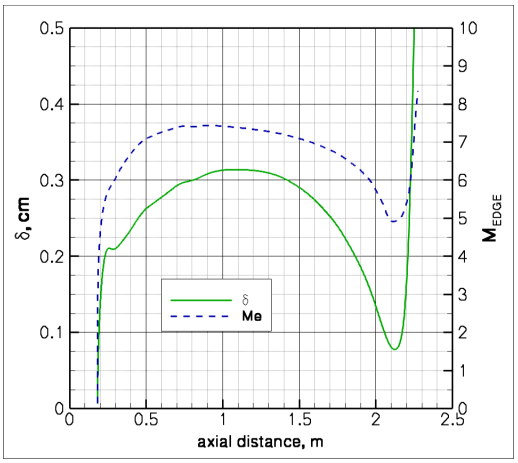

Figure 14. Boundary Layer Growth on Axisymmetric Compression Surface

A sample comparison of measured versus predicted heat transfer is shown in Fig 15 for a case for which transition occurs midway down the body. For this condition, the first several gages display laminar behavior, followed by several gages showing transitional behavior and finally several gages which correspond to the predicted turbulent level using a Spalart-Allmaras turbulence model with compressibility correction (if it can be believed for this flow). While the CFD seems to predict the laminar levels with excellent fidelity, picking the onset of transition here is more difficult than for the cone because the heat transfer naturally rises on the latter half of the model anyway due to the compression process thinning the boundary layer. In this case, it is even more imperative to rely on the statistical variance of the thin-film heat transfer measurements.

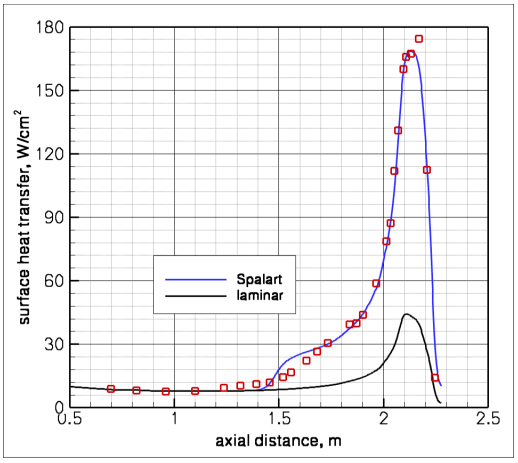

Figure 15. Comparison of Laminar and Turbulent Heat Transfer Prediction to Experimental Data for a Transitional Run (ACS-18)

Proper generation of the grid for this complex shape is especially critical for these cases. In particular, adequate resolution of the edge conditions of the boundary layer is difficult to achieve. Using a solution from a grid not properly resolved for this problem results in an estimation of edge Mach number that fluctuates wildly. To remedy this, the generation of the flowfield solution was done in two steps. First, a grid was generated by extruding normal to the surface at all points. This grid was run with the DPLR code to convergence and the grid was adapted to the shock layer using DPLR's built-in adaptation routine. The shock adaptation modifies each body-normal line of grid points to place a specified number inside the shock layer (usually all but a few of them) while preserving the orthogonality to the surface. The boundary layer thickness was then extracted from this solution and the boundary layer edge location and outer boundary lines were imported back into the grid generator to provide fine control over the distribution of grid points at the boundary layer edge. A target of 120 cells was set within the boundary layer and fine body-normal spacing used in the edge region.

C. PSE-Chem Analysis Results

As before, results from a typical run (ACS-19) are studied in detail and results are summarized for all runs in the series at the end of the section. The planner window of the STABL GUI is shown in Fig 16. The key observation for the stability of this flowfield is that the estimated second-mode disturbance instability frequency remains nearly constant at near 200kHz for almost 1-m of running length of this body. That behavior is caused by the inhibition of boundary layer growth by the adverse pressure gradient as shown already in Fig 14. This is in stark contrast to the normal trends seen for zero pressure gradient flows like the cases of the previous section where boundary layer thickness grows steadily and the corresponding instability frequency drops.

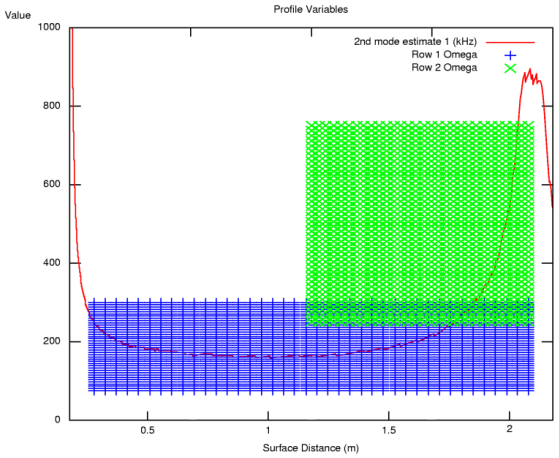

Figure 16. STABL Test Matrix for Run ACS-19

The N-factor map predicted by STABL is shown in Fig 17. The result reflects the behavior estimated by the planner tool in that instabilities around the nearly-constant second-mode frequency are allowed to grow unchecked down the length of the body starting at the X=0.6m location. This map is unlike the predicted map for a cone where individual instabilities tend to grow and then recede until overall growth reaches the onset level (as in Fig 8). Transition in the case of the axisymmetric compression surface is caused by instabilities which initiate far upstream near the nose of the model and travel nearly one meter downstream before transitional heating is experimentally observed by the surface instrumentation measurements. Transition was measured at 1.56-m which corresponds to a predicted N=8.6 as shown by Fig 18. This value is significantly higher than we observed for the cone cases and is close to the N-factors typically observed in flight. The frequency of dominant instability is 207 kHz at this location, a value that is in the middle of the values predicted by STABL on the cone cases studied so it is not immediately obvious why the larger N-factor is predicted for this case.

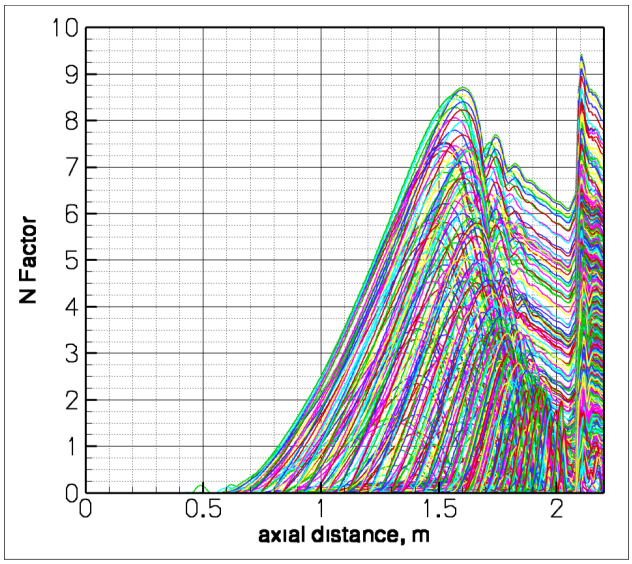

Figure 17. STABL N-Factor Instability Map for Run ACS-19

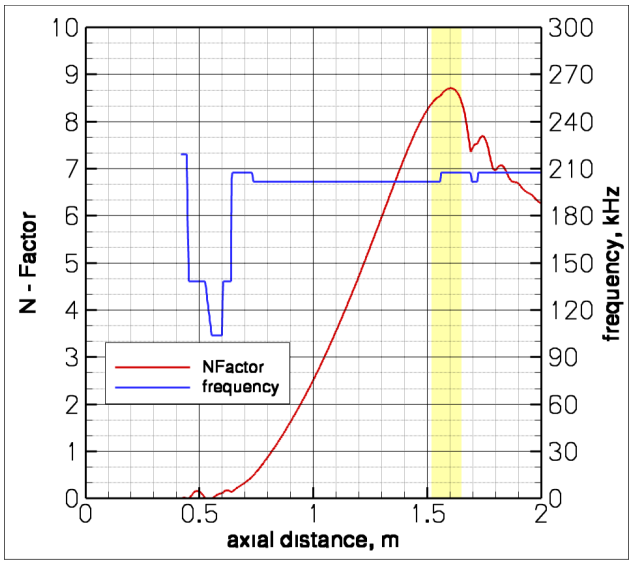

Figure 18. Instability (N-Factor) Envelope and Frequency for Run ACS-19 (transition at 1.52-1.65 m)

The summary of all axisymmetric compression cases is shown in Table 2. Runs ACS-13 through ACS-18 varied the freestream Reynolds number only while runs ACS-18 through ACS-20 show the effect of varying the nose radius while keeping freestream conditions the same. In general, the N-factors at transition for these cases, averaging 7.1 over all six runs, are higher than for the cones cases and show a larger range from lowest to highest. The frequencies of maximum instability also vary more widely although there is no obvious correlation to the N-factor. The values of Re_θ/M_E in all cases are much lower than the values observed on the cone. Again with this test series, the values of Re_θ/M_E for cases varying Reynolds number only are most consistent with each other, but little

sense can be made of this parameter for cases varying nose radius or in comparisons between the axisymmetric compression surface and the cone. In fact, looking at Re_θ/M_E alone would suggest that the axisymmetric runs transition more easily (e.g. at lower values) than the cone, while the PSE solution shows the opposite trend, requiring more disturbance amplification before transition onset occurs.

Table 2. Summary of Stability Analysis for Mach 10 Axisymmetric Compression Surface Studies

Run #	Nose radius (mm)	Freestream Mach number	Freestream unit Reynolds number x10^6 (m^{-1})	Transition location (axial) (m)	Instability N-factor at transition	Max-N Instability frequency (kHz)	Transition Point Local edge Reynolds number x10^6	Re_θ/M_E
ACS-13	1.27	9.96	1.57	1.40	7.4	155	1.54	45
ACS-16	1.27	10.00	0.72	1.75	5.7	109	1.24	39
ACS-17	1.27	10.00	1.13	1.64	7.4	130	1.56	44
ACS-18	1.27	9.98	2.87	1.23	7.5	220	2.06	54
ACS-19	3.05	9.92	2.67	1.56	8.6	207	3.31	69
ACS-20	3.81	9.97	2.87	1.70	6.2	200	4.23	77

The trend of transition N-factor amplification for the last three runs ACS-18, ACS-19, ACS-20 also require some further explanation. At first glance, the N-factor result for these three cases, which vary from 7.5 to 8.6 to 6.2 with increasing nose radius, seems random. However, the environment that the transition onset occurs in must be considered. Additionally, as shown in Fig 19, the N-factor map is strange for this case. Unlike run ACS-19, where transition onset occurs right at the peak of the disturbance growth (Fig 18), here transition onset occurs where the N-factors targeted by the second mode analysis are decaying. We have reported the peak N-factor occurring at X=1.55-m as the solution for this case, but the reality is that the computed N-factor has decreased from 6.2 to about 5.0 and is rapidly decaying in this region.

The Clauser pressure gradient parameter[34] is plotted in Fig 20 showing the three measured transition points for the three runs in this series. The pressure gradient parameter was computed numerically from the mean flow solution for run ACS-19 but, since it is non-dimensional, the trend holds for all runs. Onset for each run occurs in a region where the dimensionless pressure gradient is approximately double the value from the previous run (β~0.1, 0.2, and 0.4 for runs ACS-18, 19, and 20 respectively). The increasing pressure implies strong concave curvature in the transition region of ACS-20. We therefore suggest the possibility that the transition for ACS-20 may be by streamwise vortex instability[35] rather than by pure second-mode growth alone. We have not made a formal computational study of this effect since this work focused solely on pure second-mode transition prediction using the STABL code, but it seems logical to consider this possibility in future study of this case.

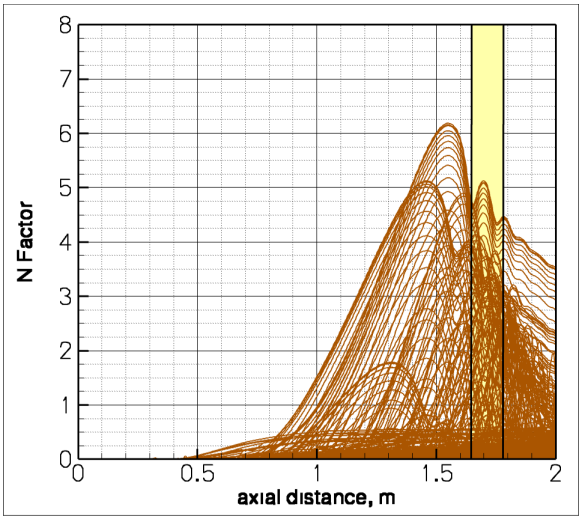

Figure 19. STABL N-Factor Instability Map for Run ACS-20 showing Transition Onset Location

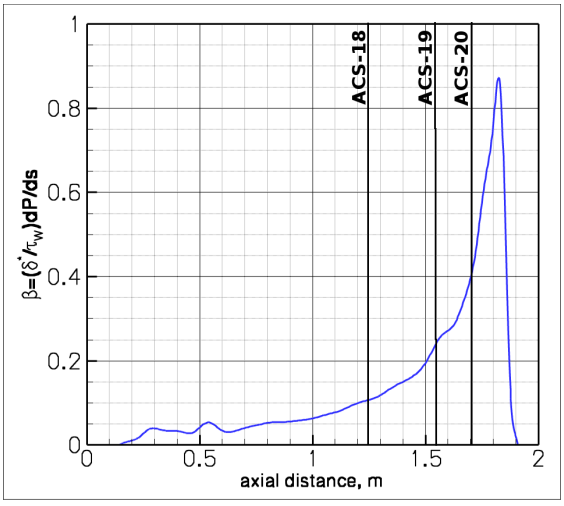

Figure 20. Clauser Pressure Gradient Parameter for ACS Flowfield Showing Nominal Transition Locations for ACS-18, 19, 20

VI. Issues Associated with Uncertainties

A. Numerical Issues

Before employing a new computational tool for applied decision-making, it is imperative to validate that tool first. Since the analysis presented here was the first time that CUBRC has employed the STABL tool in its assessment of transitional flows, it was necessary to do some basic validation early in the effort to insure that quality results could be obtained from the code. To demonstrate this, run Cone-19 from the cone dataset discussed in §IV was selected to provide freestream conditions and geometry. Comparison with the experimental results is unimportant for this purely computational verification. A high resolution grid was created consisting of 1024x512 cells that was shock-adapted and iterated to convergence with the DPLR code. This shock-adapted grid was then sequenced in both directions by factors of two and four to obtain solutions on grids of 512x256 and 256x128 cells. As before, the cell Reynolds number was controlled in the shock adaptation such that it would be about 1 in the coarsest case. The stretching of the grid points resulted in approximately 256 points in the boundary layer of the finest grid, 128 points for the medium grid, and 64 points for the coarse grid. The test matrix to target second mode transition for this case is shown in Fig 21, which was identical for all three grids and consisted of a total of 1140 test points. The comparison of the three results obtained with the unified set of test points is shown in Fig 22(a). The solutions show consistent interpretation of N-factor growth behavior at all points on the model. Small variations between the solutions are evident, particularly at the aft part of the body. However, since any differences are well within the uncertainties associated with modeling the transition process, the practical engineering interpretation of this result is that even 64 points in the boundary layer is sufficient to provide a correct result.

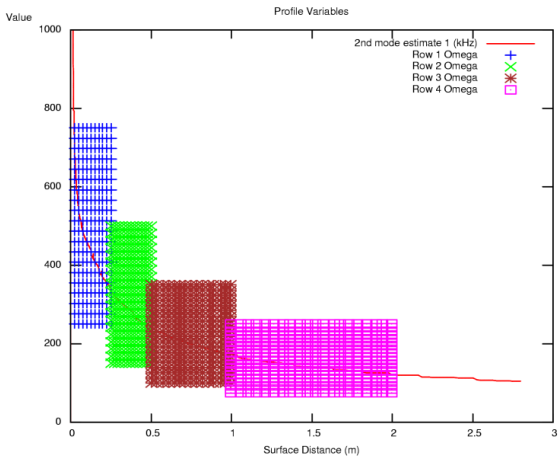

Figure 21. STABL Test Matrix for Grid Resolution Study

Next, the effect of the density of test points for the PSE solution was examined. For this part of the analysis, the medium grid (512x256) was chosen and the original test matrix of 1140 points was compared to a test matrix with exactly twice the number of axial stations and twice the number of frequencies or 4560 points. This result is shown in Fig 22(b). The effect of the increase in the number of test points is that the "valleys" in the envelope curve are filled in. The result is a smoother solution, but again the conclusion from a practical standpoint is that the interpretation of the transition location estimate is not strongly modified. Thus, we may conclude that the STABL solver provides well-behaved solution convergence in terms of both mean flow solution density and test point

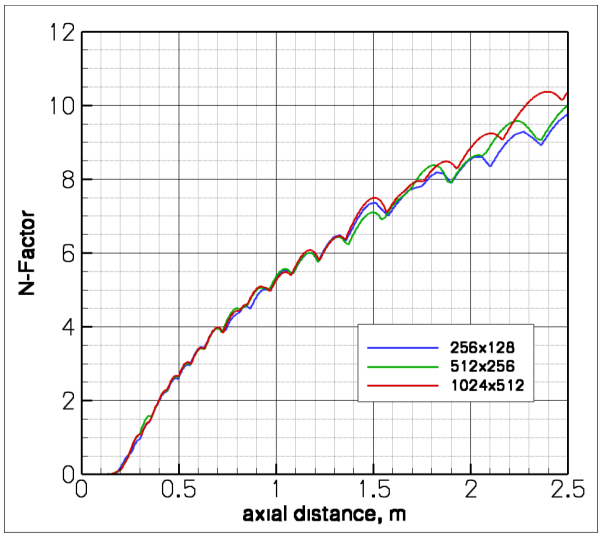

(a) Grid Sequence (Resolution)

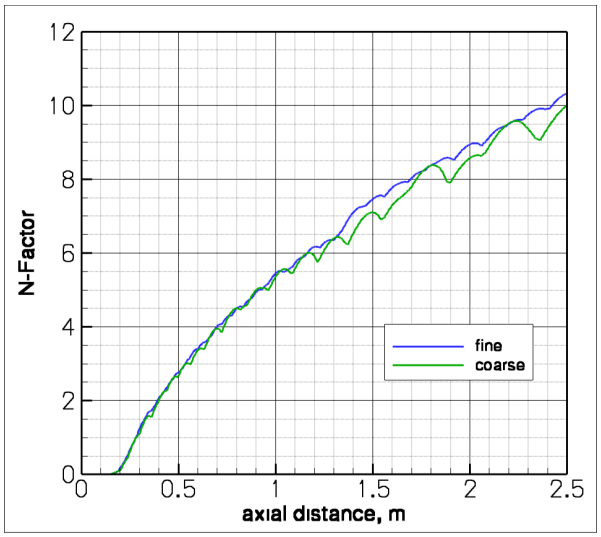

(b) Test Matrix Resolution

Figure 22. N-Factor Prediction for Grid Resolution and Test Map Resolution Studies

density. Since solutions at even the coarsest level studied are sufficient for our purposes, STABL may be considered a tool with meaningful turn-around rate that can support the experiment.

B. Experimental Issues

Experimental issues in this work deal mainly with the selection of transition onset point from the experimental dataset. Data from the experiment is in the form of heat transfer measured by thin-film gages embedded on the surface of the model. Data collected from these high-frequency response gages may be averaged over the steady-state run time to obtain the average measurement or the high-resolution temporal data can be analyzed directly. The conclusions drawn in this work require careful interpretation of the data to compare the STABL solutions to a measured transition onset point.

We have employed several methods of interpreting the data to determine transition onset. The first method is the traditional way of estimating transition onset from steady-state averaged data by drawing a trendline through the intermittent portion of the data and extrapolating to the point of zero intermittency. This estimation is shown in Fig 23 for run Cone-19. There is obviously some subjectivity about which line best fits the trend of the heating. Using the laminar DPLR solution, which fits the laminar portion of the data well, intersection occurs at a station of X=1.2m.

Because the thin-film instrumentation measures high-frequency heating with excellent accuracy, better methods of determining transition onset may be employed using this extra information. Figure 24 shows the same steady-state averaged measurements with several time history traces for selected heat transfer gages designated by the arrows. Gages in the laminar region (called out at stations 0.4m, 0.9m, and 1.05m) show a smooth behavior with little noise in the mean signal. Gages starting at the 1.2m station begin to show intermittent spikes in the mean level indicating the beginning of laminar-turbulent transition. The

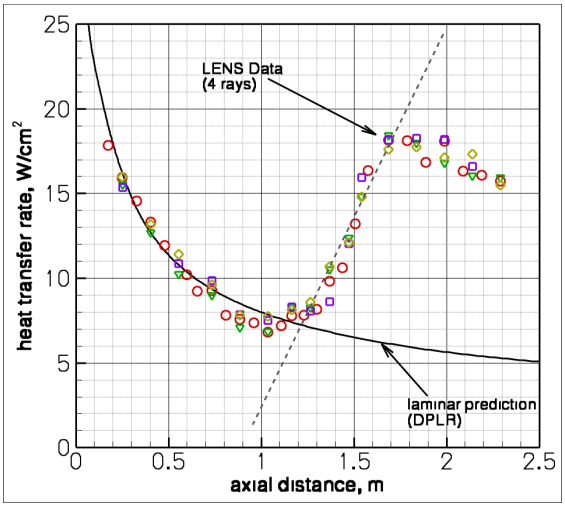

Figure 23. Estimation of Transition Onset Point for Run Cone-19 Using a Trendline to Zero Intermittency

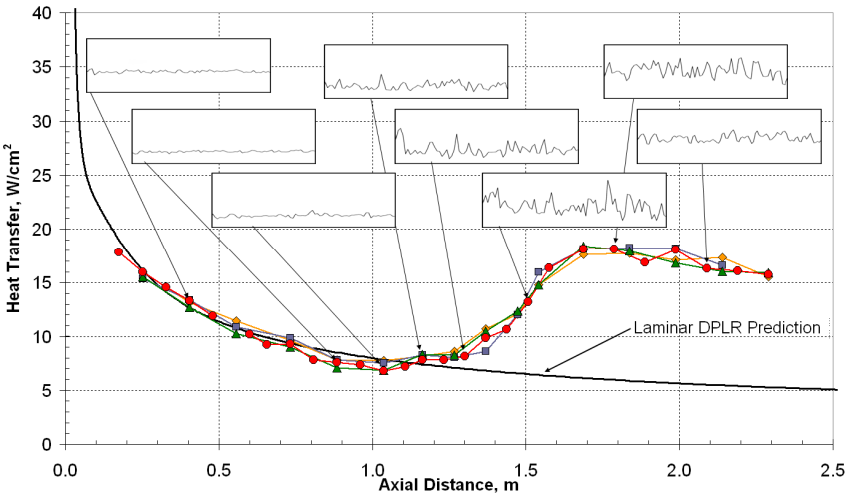

Figure 24. Estimation of Transition Onset Point for Run Cone-19 Using Thin-film Time History Traces

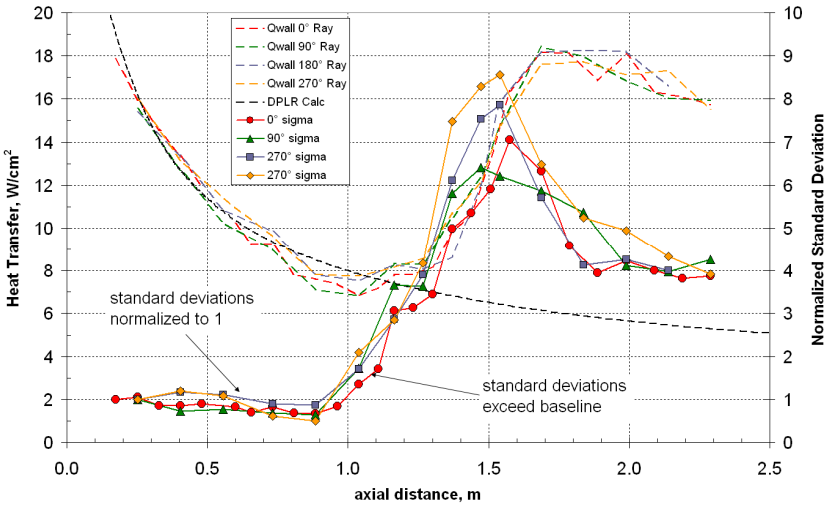

Figure 25. Estimation of Transition Onset Point for Run Cone-19 Using Thin-film Normalized Standard Deviation Correlation

frequency of these spikes increase as the level of intermittency increases. Finally, the last two traces begin to show less intermittent behavior, indicating a fully turbulent level of heating is developing.

A more quantitative technique to define the level of intermittency in the data is to compute the standard deviation of the transient signal as shown in Fig 25. The standard deviation has been normalized by the laminar level on each ray, and transition onset is apparent when the level of the standard deviation rises significantly above 1.0. This occurs at 1.05m, or just before the first visual sign of spikes in the data appears in Fig 24. As observed in the visual traces, the standard deviation of the signals reaches a maximum near the end of transition and then drops again in the turbulent region.

Since the point of transition onset is difficult to determine, a combination of all of these methods have been employed for all cases considered in this work. The range of possible onset is defined in each case by the minimum and maximum value from these methods. For run Cone-19, the possible range is 1.05-m to 1.20-m.

VII. Analysis and Discussion

The major focus of this work is in adapting the STABL simulation capability to improve the quality of the experimental studies on transition phenomena in the LENS facilities. From this perspective, the first point of discussion is in the prediction of transition onset point for design of future experiments. This capability is essential, for instance, to properly position instrumentation to capture heating trends, with particular emphasis on transitional and turbulent over-shoot heating. In the previous sections, it was shown for all eleven runs that the N-factor at transition onset varied over a range of 5.2 to 8.6 while the Re_θ/M_E parameter at the same point varied from 39 to 104. If this information is used to predict the transition location of run ACS-19, for example, the result is shown in Fig 26. Using the N-factor method, laminar-turbulent transition onset would be predicted to occur between 1.25-m and 1.60-m, a 35-cm range. Using the Re_θ/M_E metric, transition would be predicted to occur somewhere between 0.75-m and 1.98-m, a 123-cm range. Thus, the STABL solution of the PSE formulation provides three and one-half times better prediction of transition for this typical case. If the lower Mach number cases shown in Fig 5 (where values of Re_θ/M_E up to 220 were found) are included in the analysis, then the N-factor range increases only slightly while the Re_θ/M_E range would increase far beyond the end of the cone, further increasing the discrepancy in the prediction quality.

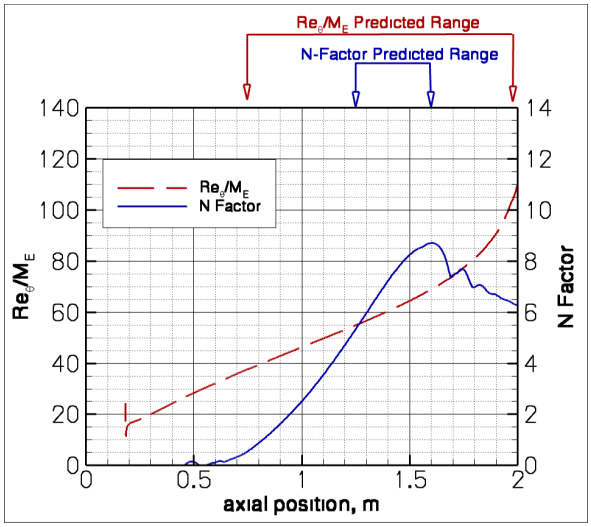

Figure 26. Comparison of Range of Transition Onset Predictions Using PSE and Re_θ/M_E Metrics

If all eleven cases are considered, the average N-factor is 6.6 and the average Re_θ/M_E is 68. These average values were used to obtain estimates of predicted local Reynolds number based on running length. These results are compared to the measured transition stations in Fig 27, where the best prediction should fall closest to the green line running diagonally through the graph. Neither method predicts all cases perfectly, but the N-factor method predictions (red and orange diamonds) are significantly better than the Re_θ/M_E predictions (blue and purple triangles). The N-factor results form an approximately linear trend, but the Re_θ/M_E results appear totally random and, if anything, seem to trend in the opposite direction than the target transition result.

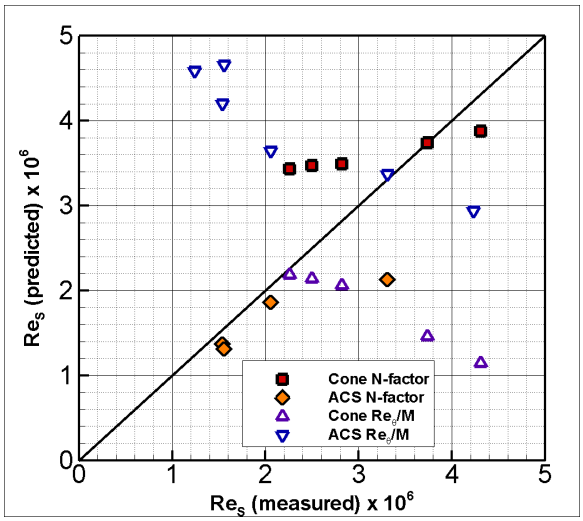

Figure 27. Predicted vs. Measured Transition Station using Average N-factor=6.6 and Re_θ/M_E=68 Methods

The STABL solution also provides a potential opportunity to assess the effects of tunnel noise on the transition onset location. Using these eleven cases, the

transition onset point N-Factor results have been plotted versus the frequency of maximum instability predicted by STABL to observe any trends in the early onset of transition with frequency. The N-factors are shown in Fig 28. It is often thought in hypersonic facilities that earliest transition onset will occur for situations where the maximum instability frequency of the model is most compatible with the frequency of noise generated by the turbulent boundary layer on the facility nozzle wall. As observed previously, the N-factors corresponding to the measured transition point for the axisymmetric compression surface cases are, in general, somewhat higher than the cone cases, although some overlap exists between the two studies. The predicted frequency of maximum instability varies over a factor of two and we can see no particular trend in the N-factors over this range. The same N-factors are also plotted versus freestream unit Reynolds number in Fig 29, which also must be related to boundary layer growth on the nozzle walls. The result is the same here, where no particular trend is obvious. The Reynolds number based on diameter in the throat of the nozzle was also computed for each of the eleven cases on the idea that this quantity might be most directly related to the frequency of noise generated as the boundary layer grows on the nozzle wall; this result produced no better correlation and is not shown. Although we understand that the differences in noise environment between ground test facilities and free-flight does reduce the disturbance amplification necessary for transition onset (after all, every case has an N-factor less than a number like 10 accepted for correlation in free-flight), the results obtained for this limited number of cases does not seem to show a direct dependence on the scaling of the turbulent boundary layer on the facility nozzle.

As pointed out by Schneider[29], Chen has also demonstrated an effect of tunnel noise with increasing nose bluntness, where transition Reynolds number remains constant instead of increasing with nose radius as it should in flight[36]. Figure 30 shows that, unlike Chen's data, our transition Reynolds number is significantly increased with an increase in nose radius, but there does seem to be some trend of increasing N-factor with nose bluntness (from Tables 1 and 2). The slope of the trend is also of a different magnitude for the two types of flowfields. It is unclear exactly what this result implies.

Given these results, we can detect no definitive resonance between the facility operating conditions and the model transition location that might refine our interpretation of the range of predicted N-factors further than 5.2 to 8.6. However, we again emphasize that the range of prediction using the STABL code is significantly better at predicting transition onset for the ground test experiments than the alternative (largely empirical or heuristic) techniques. We note that the curve of maximum N-factor versus surface distance for many of these cases has a very large slope. Thus, small changes in the measured transition location can result in large changes in

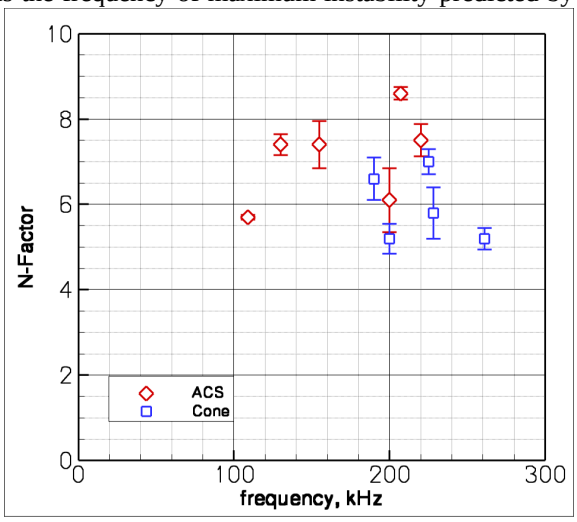

Figure 28. N-Factor at Transition Onset versus Maximum Instability Frequency

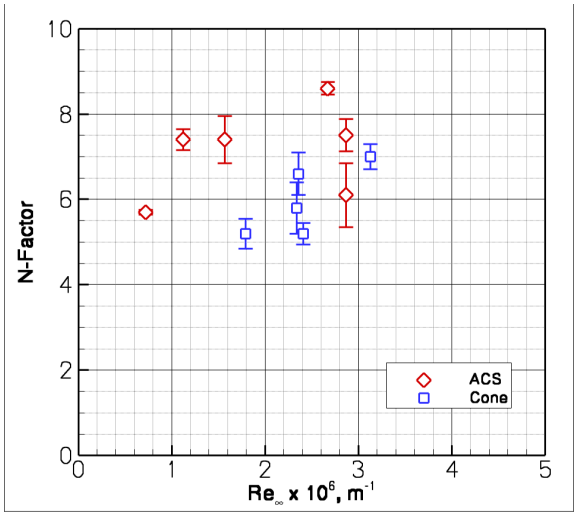

Figure 29. N-Factor at transition Onset versus Freestream Unit Reynolds Number

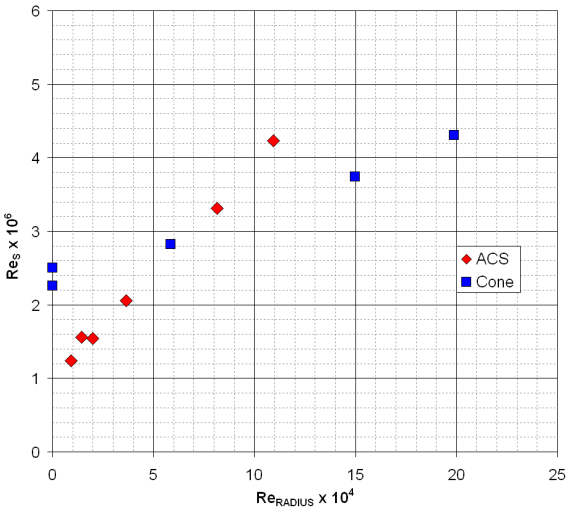

Figure 30. Effect of Increasing Nose Radius on Transition Reynolds Number

N-factor. The relatively large upper value of 8.6 and the total range of transition values are indicative of the rapid disturbance growth rate and the ability of the PSE approach to model this physical effect.

Finally, and most importantly, the issue of tunnel noise highlights the most powerful capability provided by the STABL code in terms of integration to the ground test experiment. We have shown that, in the ground test experiment, transition can be measured in multiple ways with relative accuracy in a well-controlled environment at mean-flow conditions duplicating those of flight. Using the STABL code, the stability solution can be run for the ground test case and the transition N-factor determined by comparing with the measured transition location. This value will be something less than the value of 10 expected in flight. Once calibrated, the stability solution can be used to determine how much transition onset would be moved if transition occurred at N=10 instead. This measurement, which is directly related to the slope of the maximum N-factor curve, is therefore an indication of the sensitivity of the transition location of the initial disturbance levels and allows us to make an extrapolation to the flight condition.

Two examples demonstrating this are shown in Fig 31 using runs from the cone study. In Fig 31(a), a run from the Mach 7 studies is shown, where the measured transition onset occurred at an N-factor amplification of approximately 5.2 at the 0.36-m station. From the STABL analysis, the N-factor increases to 10.0 at 0.51-m, or 15-cm downstream of the measured point. The case of run Cone-19 is revisited as shown in Fig 31(b). From Table 1, this run transitioned at a nominal station of 1.13-m with an N-factor amplification of 5.8. If N=10 is assumed, then the transition point would move from 1.13-m to 2.40-m. The disturbances amplify more slowly at the higher Mach number condition, so the adjustment from the ground test measurement is more dramatic than in Fig 31(a), but the intermittent transition process extends to nearly 2.0-m before a fully turbulent boundary layer is observed in the measurements. In both cases, this capability allows the ground test data to be extrapolated intelligently to flight. We can even account for the effect of wall temperature on the transition process, though none of the cases we have tried with STABL so far have shown much dependency with surface temperature. In this way, variations in second-mode transition onset due to tunnel noise may be accounted for on a case-by-case basis.

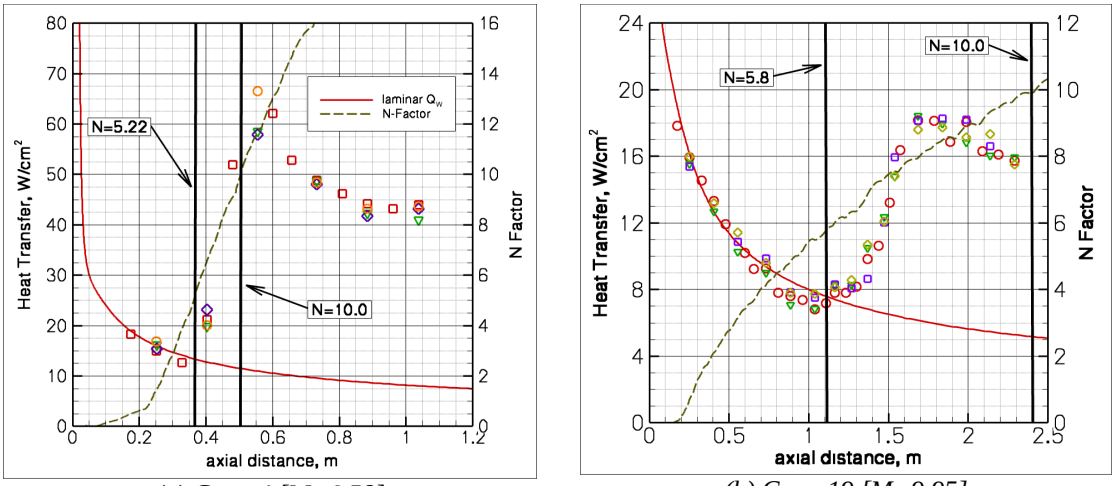

(a) Cone-4 [M=6.58] *(b) Cone-19 [M=9.95]*

Figure 31. Extrapolation of Second-Mode Transition Onset from Ground Test Environment to Flight

VIII. Conclusions

Transition studies performed in the LENS-I reflected shock tunnel facility have been analyzed to better understand second-mode dominated transition for eleven cases at a Mach 10 condition where the total enthalpy of the flow (e.g. velocity) is replicated to match the flight condition. These cases included five runs on a cone geometry with a nominally zero pressure gradient and six runs on an axisymmetric compression surface with a strong and varying adverse pressure gradient. Comparisons have been made to the measured transition locations on the models to predicted instability growth with the STABL code solving the parabolized stability equations by determining the range of N-factors predicted for the measured transition onset stations.

Comparisons on the five 7^O cone cases demonstrated N-factor growth between 5.2 and 7.0 to cause observable transition onset. This configuration creates a flow with nominally zero pressure gradient downstream of the nosetip. While the Re_θ/M_E parameter successfully correlated transition with a change in freestream Reynolds number, it showed significant changes with a change in model nosetip radius. Comparisons made for six runs on an

axisymmetric compression surface showed unexpected behavior compared to the cone. Here, N-factor growth predictions made with STABL ranged from 5.7 to 8.6, generally higher values than observed for the cone experiments. However, the values of Re_θ/M_E for this configuration ranged from 39 to 77 which were significantly lower than the values computed for the cone. Therefore, we can conclude that the correlation of transition with Re_θ/M_E between these two shapes actually leads to an incorrect conclusion about the relative stability of the boundary layer. It seems from the analysis of the data that the effect of the adverse pressure gradient on the boundary layer stability is substantial, but it is not clear why the N-factors were computed to be generally higher than on the cone. Regardless of the source of this discrepancy, the axisymmetric compression geometry proved to be an interesting case to study transition with and requires more analysis to sufficiently resolve.

In terms of ground test simulation of the transition process, the range of all eleven cases in this study yielded an N-factor growth range of 5.2 to 8.6. In all cases, the measured N-factor was at least somewhat lower than accepted values for flight, but initial efforts to correlate the magnitude of this difference with the operation of the facility were unsuccessful. In this way, it did not seem that the noise levels were present in the facility in any way that was a function of Reynolds number or any of the operating characteristics of the tunnel. Additional experiments to better resolve any trends in regard to this will provide additional confidence of the role of tunnel noise in making a PSE analysis of the ground test data.

Finally, we have adopted the STABL code as a tool with which to plan, study, and interpret the ground test data from experiments in our shock tunnel facilities and as a tool with which to directly extrapolate that data to conditions in a flight environment. The benefits of using this tool over empirical correlations for this type of analysis are threefold: (1) the uncertainty of prediction of transition onset is significantly decreased as shown by Fig 27, (2) the solutions have a physically meaningful quality to them, and (3) the analysis with the physically based PSE equations provides additional information about the transition process beyond an estimate of onset point that is not available from experiment alone. This is most clearly illustrated with the case of ACS-20 in Fig 19. Here, we observed an unexpected behavior in the STABL results that, upon further investigation, suggests that the transition process may not be occurring as a result of pure second mode growth. Although not yet proven quantitatively, this observation tells us something about the experiment that we could not have observed from the measurements alone and provides direction for future study and analysis of this type of phenomena. This initial investigation into the use of the STABL code has been successful in enhancing our interpretation of the experiment. We have found STABL to generate physically meaningful solutions at a pace that can be integrated into the experiment. Future experiments employing this tool will provide additional test points to more fully develop and verify the results shown here in this initial study.

References

[1]Holden, M.S. and Parker, R.P. “LENS Hypervelocity Tunnels and Application to Vehicle Testing at Duplicated Flight Conditions,” Chp 4 of *Advanced Hypersonic Test Facilities*. Lu, F.K. and Marren, D.E. Eds. AIAA Progress in Astronautics and Aeronautics Series: Vol 198. Chapter 4. Reston, VA: American Institute of Aeronautics and Astronautics, 2002.

[2]Holden, M.S.; Wadhams, T.P.; and Candler, G.V. “Experimental Studies in the LENS Shock Tunnel and Expansion Tunnel to Examine Real-Gas Effects in Hypervelocity Flows”. AIAA Paper 2004-0916. January 2004.

[3]Parker, R.; Wakeman, T.; Holden, M.; and MacLean, M. “Measuring NO Freestream Concentration Using Quantum Cascade Lasers at CUBRC”. AIAA Paper 2006-0926. 44TH Aerospace Sciences Meeting & Exhibit. Reno, NV: 9-12 January 2006.

[4]Parker, R.; Wakeman, T; MacLean. M.; and Holden, M. “Measuring Nitric Oxide Freestream Velocity Using Quantum Cascade Lasers at CUBRC”. AIAA Paper 2007–1329. 45TH Aerospace Sciences Meeting & Exhibit. Reno, NV: 8-11 January 2007.

[5]Wright, M.J.; Bose, D.; and Candler, G.V. “A Data Parallel Line Relaxation Method for the Navier-Stokes Equations”. *AIAA Journal*. Vol 36, no 9. Pgs 1603 – 1609. Sept 1998.

[6]MacCormack, R.W. and Candler, G.V. “The Solution of the Navier-Stokes Equations Using Gauss-Seidel Line Relaxation”. *Computers and Fluids*. Vol 17, No 1. Pgs 135 – 150. 1989.

[7]Candler, G.V. “Chemistry of External Flows”. *Aerothermochemistry for Hypersonic Technology*: Von Karman Institute for Fluid Dynamics Lecture Series. VKI LS 1995-04.

[8]Landau, L. and Teller, E. “Theory of Sound Dispersion”. *Physikalische Zeitschrift der Sowjetunion*. Vol 10, no 34. 1936.

[9]Millikan, R. and White, D. “Systematics of Vibrational Relaxation”. *Journal of Chemical Physics*. Vol 39, no 12. Pgs 3209 – 3213. 1963.

[10]Camac, M. “CO_2 Relaxation Processes in Shock Waves”. *Fundamental Phenomena in Hypersonic Flow*. J.G. Hall Ed. Cornell University Press. Pgs 195 – 215, 1964.

[11]Park, C.; Howe, J.T.; Jaffe, R.J.; and Candler, G.V. “Review of Chemical-Kinetic Problems of Future NASA Missions II: Mars Entries”. *Journal of Thermophysics and Heat Transfer*. Vol 8, no 1. Pgs 9 – 23. 1994.

[12]Park, Chul. "Assessment of Two-temperature Kinetic Model for Ionizing Air". AIAA Paper 87-1574. AIAA 22ND Thermophysics Conference. Honolulu, HI: 8-10 June 1987.

[13]Marrone, P.V. and Treanor, C.E. "Chemical Relaxation with Preferential Dissociation from Excited Vibrational Levels". *The Physics of Fluids*, Vol 6, no 9. Pgs 1215 – 1221. September 1963.

[14]Palmer, G.E. and Wright, M.J. "A Comparison of Methods to Compute High Temperature Gas Viscosity". *Journal of Thermophysics and Heat Transfer*. Vol 17, no 2. Pgs 232 – 239. 2003.

[15]Palmer, G.E. and Wright, M.J. "A Comparison of Methods to Compute High Temperature Gas Thermal Conductivity". AIAA Paper 2003-3913. Jun 2003.

[16]Gupta, R.; Yos, J.; Thompson, R.; and Lee, K. "A Review of Reaction Rates and Thermodynamic and Transport Properties for an 11-Species Air Model for Chemical and Thermal Nonequilibrium Calculations to 30000 K". NASA RP-1232. August 1990.

[17]Ramshaw, J.D. "Self-consistent Effective Binary Diffusion in Multicomponent Gas Mixtures". *Journal of Non-Equilibrium Thermodynamics*. Vol 15, no 3. Pgs 295 – 300. 1990.

[18]Baldwin, B.S. and Lomax, H. "Thin Layer Approximation and Algebraic Model for Separated Turbulent Flows". AIAA Paper 78-0257. Huntsville, AL: 1978.

[19]Spalart, P.R. and Allmaras S.R. "A One-Equation Turbulence Model for Aerodynamic Flows". AIAA Paper 92-0439. 30TH Aerospace Sciences Meeting & Exhibit. Reno, NV: 6-9 Jan, 1992.

[20]Menter, F.R. "Two-Equation Eddy-Viscosity Turbulence Models for Engineering Applications". *AIAA Journal*. Vol 32, no 8. Pgs 1598 – 1605. August 1994.

[21]Brown, James. "Turbulence Model Validation for Hypersonic Flow". AIAA Paper 2002-3308. 8TH Thermophysics and Heat Transfer Conference. St. Paul, MN: 24 – 26 Jun 2002.

[22]Catris S. and Aupoix B. "Improved Turbulence Models for Compressible Boundary Layers." AIAA Paper 98-2696. 2ND Theoretical Fluid Mechanics Meeting: Albuquerque, NM, June 1998.

[23]Saunders, D.; Yoon, S.; and Wright, M. "An Approach to Shock Envelope Grid Tailoring and Its Effect on Reentry Vehicle Solutions," AIAA Paper 2007-0207. 45TH Aerospace Sciences Meeting & Exhibit. Reno, NV: 8-11 January 2007.

[24]Johnson, Heath B. *Thermochemical Interactions in Hypersonic Boundary Layer Stability*. Ph.D. Thesis, University of Minnesota, Minneapolis, MN, 2000.

[25]Johnson, H. and Candler, G. "Hypersonic Boundary Layer Stability Analysis Using PSE-Chem." AIAA Paper 2005-5023. 35TH AIAA Fluid Dynamics Conference and Exhibit, Toronto, ON. June 2005.

[26]Johnson, H. and Candler, G. "Analysis of Laminar-Turbulent Transition in Hypersonic Flight Using PSE-Chem." AIAA Paper 2006-3057. 36TH AIAA Fluid Dynamics Conference and Exhibit, San Francisco, CA. 5 – 8 June 2006.

[27]Herbert, T. "Boundary Layer Transition – Analysis and Prediction Revisited." AIAA Paper 91-0737. January, 1991.

[28]Johnson, H.; Alba, C.; Candler, G.; MacLean, M.; Wadhams, T.; and Holden, M. "Boundary Layer Stability Analysis to Support the HiFiRE Transition Experiment". AIAA Paper 2007 – 0311. 45TH Aerospace Sciences Meeting & Exhibit. Reno, NV: 8-11 January 2007.

[29]Schneider, S. "Effects of High-Speed Tunnel Noise on Laminar-Turbulent Transition," *Journal of Spacecraft and Rockets*. Vol 38, no 3. Pgs 323 – 333. May – June 2001.

[30]Kimmel, R.; Schwoerke, S.; and Klein, M. "Three-Dimensional Hypersonic Laminar Boundary Layer Computations for Transition Experiment Design," AIAA Paper 96-2080. June 1996.

[31]Papadopoulos, P.; Venkatapathy, E.; Pradhu, D.; Loomis, M.; and Olynick, D. "Current Grid-generation Strategies and Future Requirements in Hypersonic Vehicle Design, Analysis and Testing". *Applied Mathematical Modeling*, Vol 23. Pgs 705 – 735. 1999.

[32]Reshotko, E. "Is Re_θ/M_e a Meaningful Transition Criterion?" AIAA Paper 2007-0943. 45TH Aerospace Sciences Meeting & Exhibit. Reno, NV: 8-11 January 2007.

[33]Molder, S.; McGregor, R.J.; and Paisley, T.W. *A Comparison of Three Hypersonic Air Inlets*. Ryerson Polytechnic Institute School of Aerospace Engineering Contract Report (Ryerson Library Call # TL573.M65 1991). Toronto, ON, Canada. July 1991.

[34]Clauser, F.H. "Turbulent Boundary Layers in Adverse Pressure Gradients". *Journal of the Aeronautical Sciences*. Vol 21. Pgs. 91–108. 1954.

[35]Saric, W. "Görtler Vortices." *Annual Review of Fluid Mechanics*. Vol 26. Pgs 379 – 409. 1994.

[36]Chen, F.J. "Boundary-Layer Transition Extent Measurements on a Cone and Flat Plate at Mach 3.5," AIAA Paper 93-0342. January 1993.